Article:
Mata, CP, Mertens, J, Fontana, J orcid.org/0000-0002-9084-2927 et al. (7 more authors) (2018) The RNA-binding protein of a double-stranded RNA virus acts like a scaffold protein. Journal of Virology, 92 (19). 00968-18. ISSN 0022-538X

https://doi.org/10.1128/JVI.00968-18

The RNA-binding protein of a double-stranded RNA virus acts like a scaffold protein

Carlos P. Mata[a,*], Johann Mertens[b], Juan Fontana[c,†], Daniel Luque[a,d], Carolina Allende-Ballestero[a], David Reguera[e], Benes L.Trus[f], Alasdair C. Steven[c], José L. Carrascosa[a,g,#] and José R. Castón[a,g,#]

[a]Department of Structure of Macromolecules, Centro Nacional de Biotecnología (CNB-CSIC), Campus Cantoblanco, Madrid, Spain; [b]Instituto Madrileño de Estudios Avanzados en Nanociencia (IMDEA Nanociencia) Campus Cantoblanco, Madrid, Spain; [c]Laboratory of Structural Biology Research, National Institute of Arthritis, Musculoskeletal and Skin Diseases, National Institutes of Health, Bethesda, Maryland, USA; [d]Centro Nacional de Microbiología/ISCIII, Majadahonda, Madrid, Spain; [e]Departament de Física de la Matèria Condensada, Facultat de Física, Universitat de Barcelona, Barcelona, Spain; [f]Imaging Sciences Laboratory, CIT/NIH, Bethesda, Maryland, USA; [g]Unidad Asociada de Nanobiotecnología CNB-CSIC/IMDEA, Cantoblanco, Madrid, Spain

Running title: RNA-binding protein as scaffolding protein

[*]Present address: MRC Laboratory of Molecular Biology, Cambridge, UK

[†]Present address: Astbury Centre for Structural Molecular Biology and School of Molecular and Cellular Biology, University of Leeds, Leeds, UK

[#]Co-corresponding authors; correspondence to: José R. Castón, jrcaston@cnb.csic.es and José L. Carrascosa, jlcarras@cnb.csic.es

Keywords: cryoEM and cryoET/dsRNA-binding protein/IBDV/scaffolding protein/virus assembly

Word count abstract: 179; text: 5,149

Abstract

Infectious bursal disease virus (IBDV), a non-enveloped, double-stranded (ds)RNA virus with a T=13 icosahedral capsid, has a virion assembly strategy that initiates with a precursor particle based on an internal scaffold shell similar to that of tailed dsDNA viruses. In IBDV-infected cells, the assembly pathway results mainly in mature virions that package four dsRNA segments, although minor viral populations ranging from zero to three dsRNA segments also form. We used cryo-electron microscopy, cryo-electron tomography and atomic force microscopy to characterize these IBDV populations. The VP3 protein was found to act as a scaffold protein by building an irregular, ~40 Å-thick internal shell without icosahedral symmetry, which facilitates formation of a precursor particle, the procapsid. Analysis of IBDV procapsid mechanical properties indicated a VP3 layer beneath the icosahedral shell, which increased effective capsid thickness. Whereas scaffolding proteins are discharged in tailed dsDNA viruses, VP3 is a multifunctional protein. In mature virions, VP3 is bound to the dsRNA genome, which is organized as ribonucleoprotein complexes. IBDV is an amalgam of dsRNA viral ancestors and traits from dsDNA and single-stranded (ss)RNA viruses.

Importance

Structural analyses highlight the constraint of virus evolution to a limited number of capsid protein folds and assembly strategies that result in a functional virion. We report cryo-EM and cryo-electron tomography structures and atomic force microscopy studies of the infectious bursal disease virus (IBDV), a double-stranded RNA virus with an icosahedral capsid. We found evidence of a new inner shell that might act as an internal scaffold during IBDV assembly. The use of an internal scaffold is reminiscent of tailed dsDNA viruses, which constitute the most successful self-replicating system on Earth. The IBDV scaffold protein is multifunctional and, after capsid maturation, is genome-bound to form ribonucleoprotein complexes. IBDV encompasses numerous functional and structural characteristics of RNA and DNA viruses; we suggest that IBDV is a modern descendent of ancestral viruses, and comprises different features of current viral lineages.

Introduction

Structural information related to the capsid protein (CP) has become crucial for identifying phylogenetic relationships among viruses (1). Based on their CP fold, viruses are grouped into a limited number of structure-based lineages (2). Four lineages have been established to date; these are (i) the dsDNA viruses, with an upright double β-barrel CP (prototypes are phage PRD1 and adenovirus), (ii) the tailed dsDNA phages, tailed haloarchaeal viruses, and herpesviruses, which all share the Hong Kong 97 (HK97)-like CP fold, (iii) the picornavirus-like superfamily, with a single horizontal β-barrel as the CP fold (3), and (iv) the dsRNA or bluetongue virus (BTV)-like viruses. Most of these lineages include icosahedral viruses, although poxviruses are linked to the PRD1-like lineage (4, 5).

The similarity of the CP fold and virion architecture within the same viral lineage entails additional resemblance of structural components related to virion assembly (6) and genome packaging (7). Minor or transient participants such as cementing proteins, portal or genome (dsDNA)-packaging proteins, and scaffold proteins (SP) function with the CP as a structural module encoded by a fixed group of genes (8). Viruses of the HK97-like lineage, although they have variety of replication, share the same virion assembly principles. HK97-like virions assemble as a precursor particle, the procapsid, which subsequently expands to a mature capsid during genome packaging (9). CP assembly requires SP or its functional equivalent; viral expansion is initiated by genome packaging and is associated in some cases to the action of a protease in the capsid interior that cleaves SP. The portal complex, which is incorporated at the onset of capsid assembly, is responsible for viral genome encapsidation and includes an ATP-driven nanomotor; it is also found in the PRD1-adenovirus lineage (10). In the picornavirus-like superfamily that includes ssRNA viruses, CP assembly takes place around the viral genome in a coupled assembly-packaging process.

Most dsRNA viruses share a multishelled icosahedral capsid, in which the innermost T=1 icosahedral capsid provides a platform for RNA transcription and replication (11-13). The T=1 capsid has 120 copies of a platelike protein, in which the CP fold is the hallmark of the BTV lineage, that nucleate around genomic ssRNA copies (14, 15). The inner shell acts a template to prime the assembly of the T=13 surrounding capsids.

We analyzed the capsid assembly of the birnavirus infectious bursal disease virus (IBDV), a non-enveloped, icosahedral dsRNA virus (16, 17). Birnaviruses are exceptions, as they lack the 120-subunit T=1 core (16, 18); instead, they have a single ~70-nm-diameter T=13l icosahedral capsid that encapsidates a polyploid bipartite dsRNA genome (segments A and B; 3.2 and 2.8 kbp, respectively), organized as ribonucleoprotein complexes (RNP) (19, 20). The CP VP2 is synthesized as a precursor (pVP2) within a polyprotein that also includes the protease VP4 and the multifunctional protein VP3 (21, 22). In addition to its RNA-binding activity (20, 23, 24), VP3 interacts with itself (25), with the viral polymerase (4, 26, 27), and/or with pVP2 (17, 28). The proteolyzed pVP2 C terminus bears the α5-helix (17, 29), a conformational switch responsible for the inherent VP2 polymorphism. The VP3 C terminus interacts with the α5-helix to modulate the structural polymorphism of VP2; VP3 has thus been suggested as a scaffold protein during capsid morphogenesis (17).

Whereas IBDV RNP and genome polyploidy are common among negative ssRNA viruses (30), the VP2 fold has structural similarities to other picornavirus-like CP (16), as it is notably similar to CP of noda- and tetraviruses (31, 32). Here we found that IBDV capsid assembly has a structural framework like that of HK97-like lineage viruses. In genome-lacking virion particles, the VP3 forms a flexible inner shell that could act as a scaffold, and functions as an RNA-binding protein in mature virions.

Results

Cryo-electron tomography of natural IBDV populations. In IBDV-infected cells, up to six extracellular viral particles (E1-E6) can be purified by ultracentrifugation in CsCl gradients (Fig 1A), based on the copy number of packaged dsRNA segments. Virions that package four RNP (viral particles E5-E6) are nonetheless the most abundant and make up 64% of total particles. E2-E6 are T=13 capsids with a similar protein composition (Fig 1B), with increasing RNP content from 1, 2, 3 (for E2, E3 and E4, respectively) to 4 dsRNA segments. E1 particles are empty and, in addition to T=13 capsids (~70 nm diameter), include T=7 (~53 nm) and T=1 (~26 nm) capsids, CP helical assemblies, and partially broken capsids (17). Due to this structural heterogeneity, E1 global stoichiometry differs from that of E2-E6 particles (for example, E1 T=1 capsids are built only of VP2 trimers).

To analyze the organization of IBDV particle internal content, we used cryo-electron tomography (cryo-ET) to generate density maps of individual particles. A total of 46 tomograms were reconstructed (Fig 2A, B; see Movies S1 and S2 in the supplemental material). Detailed inspection of central sections of individual particle tomograms (with no imposed symmetry) indicated that ~50% of the E1 T=13 capsids showed increased, irregular thickness of the capsid wall, with an internal density similar to the background (i.e., empty) (Fig 2Ci to iii). Minor E1 particles were empty (14%; Fig 2Civ) or had a homogeneous internal density (36%) that might reflect contaminating RNP-containing capsids (Fig 2Cv). Although the capsid shell appeared to have considerable icosahedral symmetry (indicated by the hexagonal and pentagonal profiles), the underlying layer is variable and probably asymmetric (although it might be distorted during particle purification). E2-E6 particles showed increased internal content, but no structural pattern was identified (Fig 2D). A total of 1,517 particles were extracted and, for each IBDV population, icosahedral orientations were

128 determined and maps were averaged (see Methods). The resolutions achieved based on a 0.5
129 Fourier shell correlation (FSC) threshold were ~50 Å.
130 The outer surface of the E1-E6 capsids showed the T=13l geometry (Fig 2E, F). E1-E6
131 T=13 particle diameters were identical, as determined from spherically averaged radial
132 density plots of three-dimensional reconstructions (3DR) (Fig 2G). After imposition of
133 icosahedral symmetry, E2-E6 internal content was distributed homogeneously (Fig 2G,
134 dashed lines) and, as predicted, density was greater than that in E1 particles (Fig 2G, red
135 line). The inner surface of the E2-E6 protein shells was clearly separated from the underlying
136 density ascribed to encapsidated RNP. The inner surface of the E1 protein shell nonetheless
137 had extensive interactions with inner densities centered at a radius of ~225 Å. This was
138 reflected in the smaller Fresnel ring (~250 Å radius) on the E1 capsid inner surface (Fig 2G,
139 arrow). Based on analysis of the radial density distribution of the E1 capsid, the density
140 beneath the E1 capsid was delimited and its average thickness estimated to be ~40-50 Å.
141 Based on these findings, we carried out a detailed characterization of the internal density of
142 the E1 T=13 capsid, which lacks dsRNA.
143 **Biochemical analysis and cryo-electron microscopy of the empty E1 capsid: the IBDV**
144 **procapsid-like assembly.** As E1 empty assemblies are heterogeneous, we optimized T=13
145 capsid purification by pooling several E1 fractions, which were ultracentrifuged in a linear
146 sucrose gradient. Gradient fractions were characterized by SDS-PAGE and Western blot
147 (Fig 3A-C), and by electron microscopy and negative staining (Fig 3D). Whereas the middle
148 fractions (fractions 6-8) were enriched in T=13 capsids (Fig. 3D, center), top fractions (10-
149 11) contained T=1 capsids (Fig 3D, right). T=13 capsids comprised three major proteins,
150 pVP2, VP2 and VP3, observed as ~52, ~43 and ~34 kDa bands, respectively; T=1 capsids
151 had mainly VP2 (Fig 3A). Protein identity was confirmed by analysis of sucrose gradient

fractions by SDS-PAGE and Western blot using rabbit anti-VP2 (Fig 3B) and -VP3 sera (Fig 3C). The results showed that, in the absence of any other viral protein, the inner density layer adjacent to the inner capsid shell is probably built of VP3, indicating its scaffold role in situ. We used stoichiometric analysis based on Coomassie blue-stained fractions 6-8 to calculate the molar ratio between the pVP2 and VP2 bands. Anti-VP2 sera recognized a minor, intermediate, processed pVP2 band between pVP2 and VP2 (39) (Fig. 3B). The E1 T=13 capsid had a 1:1 pVP2:VP2 ratio, indicating incomplete pVP2 processing. Based on these features, we suggest that E1 T=13 capsids are a byproduct reminiscent of maturation and assembly intermediates or, in other words, the IBDV procapsid-like assemblies.

We analyzed E1 T=13 particles by cryo-electron microscopy (cryo-EM). In accordance with our previous cryo-ET analysis, visual inspection confirmed two classes of particles, E1-1 capsids (5,565 images) characterized by an empty central region and irregular capsid wall thickening (Fig 3E, red arrows), and E1-2 capsids (6,565 images) with uniform internal density (Fig 3E, blue arrows). Particles were classified by 2D and 3D analysis; based on the organization level of the VP3 inner layer, we defined two E1-1 subclasses, the E1-1A capsid (2,095 images) with many connections between the VP3 shell, and the T=13 layer inner surface (Fig 3F and 3G, left) and E1-1B (2,027 images) (Fig 3F, and 3G, middle). The E1-2 final map (2,377 images) had a VP3-related internal density distributed uniformly in its interior (Fig 3F and 3G, right). Radial density profiles of the E1-1A map showed that the VP3 layer underlying the VP2 T=13 capsid is on average ~4 nm thick (Fig 3F). The minor density of the E1-1B and E1-2 maps might result from low copy number of bound VP3 and/or from pVP2 unprocessed C-terminal ends. The three E1 capsid profiles, based on VP3 internal organization, were reproduced computationally with the 3D maps (Fig 4).

Location of (p)VP2 and VP3 in E1 and E5 T=13 capsids by immunoelectron microscopy.

176 The location of pVP2/VP2 and VP3 on E1 T=13 particles, as well as E5 T=13 capsids, was
177 also determined using immunogold labeling. Labeling anti-VP2 antiserum was clearly visible
178 around the T=13 icosahedral structures (Fig. 5A and D, left), which blurred the peripheral
179 edges of IBDV particles (compare Figs. 5A and D and Fig. 3D). This is due to the abundant
180 immune complexes that surround these particles. Tests of preimmune antisera (internal
181 controls) showed no labeling. In contrast to VP2, when the same experiment was performed
182 with anti-VP3 antiserum (Figs. 5A and D, right), no labeling was observed. This result
183 suggests that VP3 is not present or is inaccessible in these particles. To test these hypotheses,
184 the fractions were embedded in Lowicryl HM20 resin; in thin sections of this resin, capsid
185 antigenicity is well preserved and internal inaccessible epitopes (inaccessible from the
186 outside) would be exposed. Transverse sections of capsids were observed after labeling with
187 polyclonal anti-VP2 or -VP3 antibody. Anti-VP2 labeled spherical/icosahedral particles (Fig.
188 5B and E), which were not labeled by the preimmune serum. Anti-VP3 (Fig. 5C and F)
189 showed positive VP3 labeling in the E1 and E5 T=13 capsids. These data strongly suggest
190 that VP3 is not exposed on the E1 T=13 capsid surface, and that it builds the innermost shell
191 beneath the pVP2/VP2 layer, thus becoming accessible to antibodies only in sectioned
192 particles.
193 **Mechanical properties of IBDV T=13 procapsid and T=1 subviral particle.** Additional
194 evidence for the presence of VP3 as a genuine concentric layer beneath the T=13 capsid arose
195 from atomic force microscopy (AFM) experiments. We used AFM nanoindentation to
196 measure the rigidity of empty T=13 and T=1 capsids. T=1 capsids were analyzed twice, from
197 the E1 fraction (T=1 and T=13 co-purify in CsCl gradients and, based on their heights, are
198 easily distinguished) and from VP2 (441 residues) expression in the absence of other IBDV
199 components in a recombinant baculovirus system (18). Results were very similar in both

200 cases, which ruled out any relevant structural/mechanical difference. We performed 193
201 indentations for 33 E1 T=13 particles, and 170 indentations for 29 T=1 particles. The spring
202 constants, k, of the E1 T=13 and T=1 capsids were calculated from their slope histograms
203 (Fig. 6A, B). Although capsid size is quite different, rigidity was similar, as $K_{E1\text{-}T=13} = 0.347 \pm$
204 0.104 N/m and $K_{T=1} = 0.327 \pm 0.085$ N/m (for E1 T=1 capsids, $K_{E1\text{-}T=1} = 0.309 \pm 0.127$ N/m,
205 from 73 indentations for 13 T=1 capsids). The relatively broad distribution of rigidity slopes
206 from indentation experiments with individual intact E1 T = 13 capsids could account for their
207 structural variability. This result would not be anticipated if both capsids were built
208 exclusively of a similar VP2 protein layer since, according to continuum elasticity theory, the
209 spring constant is inversely proportional to capsid radius.
210 To resolve this apparent paradox, we implemented finite element (FE) simulations of
211 capsid deformation by mimicking AFM nanoindentation experiments (see Methods) (33, 34).
212 In the FE simulations, the E1 T=13 and T=1 capsids were modeled as homogeneous spherical
213 shells with an external radius, r, and thickness, h, derived from cryo-EM and X-ray data. The
214 external radius and thickness of the spherical shell representing the empty T=1 capsid were
215 r = 13 nm and h = 8 nm (Fig. 6C, left inset). A value of Young's modulus E = 120 MPa was
216 selected to yield the same spring constant in the simulations as that measured experimentally
217 for the T=1 capsid. The E1 T=13 capsid (Fig. 6C, right inset) was modeled initially as a
218 spherical shell with r = 35 nm and the same Young's modulus (E = 120 MPa) and thickness
219 (h = 8 nm) as the T=1 capsid, to ascertain the spring constant of a T=13 particle built
220 exclusively of a VP2 protein layer. The indentation curves for the 8-nm-thick T=1 and T=13
221 capsids are shown in Fig. 6C (T=1 capsid, black; T=13 capsid, red). At difference from the
222 AFM experiments, the spring constant of a T=13 shell with the same thickness as the T=1
223 particle was notably smaller. These results suggested an additional internal protein layer that

224 increases capsid rigidity. FE simulations for the E1 T=13 capsid were repeated using the
225 same external radius with varying thickness. A total thickness of 11.5 nm was needed to yield
226 an E1 T=13 capsid with a spring constant that matched that of the empty T=1 capsid (Fig. 6C,
227 green line). Assuming the same Young's modulus for T=1 and T=13 capsids, their similar
228 experimental spring constants are thus due to an ~3.5 nm thick protein layer below the VP2
229 layer in the E1 T=13 capsid, which supports our inferences from cryo-ET and cryo-EM
230 analyses of the E1 T=13 capsids.
231

Discussion

The virus genetic program is directed to produce multiple copies of infectious particles, although the ratio of defective particles during the replication cycle varies greatly (35). For IBDV, we showed direct correlation between the number of packaged RNP and particle infectivity; 96% of total infectivity is thus assigned to the E5-E6 virus population (64% of total particles, with 4 RNP/particle) (19). The E1-E4 populations are probably incorrectly assembled intermediates or abortive assemblies, a result of assembly pathway failure at longer post-infection times, when the host is severely impaired.

Our cryo-ET and cryo-EM analyses of IBDV populations demonstrated that E1 capsids bear a somewhat smaller, less ordered inner shell closely connected to the T=13 capsid inner surface. Our studies suggest that the empty E1 capsid is an assembly that resembles the IBDV procapsid. This is evidence that the RNA-binding VP3 protein can act as a SP by building a micellar-like layer in the IBDV procapsid-like E1 particles. In addition to recruiting CP during assembly and to directing fidelity and correct capsid size, the VP3 layer provides a defined set of mechanical properties to the capsid shell, as shown by our AFM indentations of empty T=13 and T=1 capsids. The additional internal VP3 layer increases procapsid-like rigidity, that is, it reduces excessive T=13 procapsid flexibility that might compromise productive virus capsid assembly.

At initial capsid assembly stages, VP3-pVP2 contacts are necessary, which could be due to the instability of the immature T=13 capsid. The relatively constant VP3 copy number [~450 VP3 copies from the E2-E6 populations (19)], which is independent of the number of packaged dsRNA segments, suggests that VP3 incorporation is determined by its role as a SP. In T=13 capsids purified from E1 fraction (Fig. 3A, fractions 6-8), pVP2 and VP2 are at a 1:1 ratio, which indicates that these capsids can be considered procapsids that require pVP2

maturation to become fully icosahedral capsids such as those of infectious IBDV virions. Based on IBDV-related assemblies generated using various baculovirus-based expression systems, we showed that electrostatic interactions between pVP2 and VP3 are important in the assembly of T=13 VLP; acid residues at the VP3 C terminus interact with the basic residues of the pVP2 amphipathic α5-helix (28).

The classification methods for the structural analysis of E1 particles resolved three particle classes probably related to assembly and/or maturation phases. The double-layered E1-1A particle shares many similarities with the herpesvirus procapsid, particularly with its B-capsid (36), a dead-end side particle in which the SP layer remains at the T=16 capsid interior with several proteases (37). In addition to the mature VP2 B domain (built of N- and C-terminal α-helices) facing the capsid interior, the E1 procapsid-like inner surface is lined with the 71-residue pVP2 C-terminal domain that includes at least four α-helices and the disordered regions of the C-terminal-most residues (29, 38). These loops, together with the high α-helical content, might be a suitable interface for SP binding to initiate procapsid assembly. The labile E1-1A capsid matures to the E1-1B capsid and CP-CP connections become more robust, whereas CP-SP connections tend to disappear. In the E1-2 capsid, most VP3 is completely disengaged from the capsid and distributed homogeneously in the capsid interior; in vivo, VP3 would be bound to the viral genome.

These dynamic assembly states might coexist in the same particle. Once virions are nearly or recently assembled as provirions, VP3 probably stops its scaffold function when the pVP2 C-terminal region is proteolyzed during virus maturation by VP4, by the host protease purSA (39), or by VP2 itself (40). VP3 then becomes an RNA-binding protein. When VP3 is bound to the viral dsRNA genome in mature virions, it also mediates capsid stability by acquiring a conformation able to interact with the mature VP2 (without helix α5), which involves a new

set of dynamic interactions between VP2 and VP3 (41). VP3 thus is able to interact with VP2 and with the dsRNA in the mature E5 particle. The battery of proteases that acts mainly on the pVP2 shell might trigger major conformational changes that transform the unstable capsid into a robust infectious particle (6).

As IBDV lacks an ATP-driven pump for genome translocation (and there is no candidate protein), the genome has to be incorporated early in the nascent capsid. Considering that VP3 might function as an adaptor molecule between the capsid shell and the viral genome, dsRNA genomic segments or their corresponding ssRNA molecules and its associated VP3 molecules can act together as a scaffold for the CP, i.e., capsid assembly and packaging of the genome are concomitant, as in many ssRNA viruses (42). VP3 might bind to the viral ssRNA of IBDV A and B segments, as in other dsRNA viruses (14, 15). Although E1 particles possibly represent unsuccessful viral assemblies (VP3 only as a SP without bound RNA), they allowed visualization of the VP3 layer as a scaffold bound to the capsid shell. . We do not rule out that genome encapsidation could be mediated by VP3-VP1 interactions (43), as a VP1 fraction is covalently bound to dsRNA (20). The multiple VP3 binding activities during capsid assembly and genome packaging might then be either sequential or simultaneous.

In IBDV and birnaviruses in general, the CP is encoded as a precursor within the polyprotein. The genomic module for IBDV capsid assembly includes the CP, the VP4 protease (21, 22) and the VP3 SP (17, 28). This organization is similar to many HK97-like viruses (except that the portal complex is lacking), but VP2 shares the fold of picorna-like rather than HK97-like CP. The picorna-like positive ssRNA viruses do not require a SP, as their capsids are much simpler than the T=13 of IBDV (3). IBDV thus resembles a hybrid of picorna- (CP fold) and HK97-like viruses (SP and procapsid). HK97- and PRD1-like viruses have an empty procapsid and a packaging ATPase (7, 10, 44), and are more closely related to

each other than to IBDV. Additional data are needed to discern whether SP-mediated assembly is indicative of an evolutionary link or is a consequence of mechanical and structural constraints.

Like the SP of many HK97-like viruses, VP3 has a pivotal function in the IBDV capsid assembly pathway. The herpesvirus- or HK97-like SP are nonetheless expelled from the procapsid during maturation, intact or degraded (45, 46). Once its role in procapsid assembly has concluded and pVP2 interaction is no longer needed, the multifunctional VP3 protein switches to an RNA-binding function, in which VP3 might interact with itself and/or activate the VP1 polymerase, thus extending its central role in the virus life cycle. In the mature virion, VP3 is bound to dsRNA, and RNP reinforces virus rigidity through a set of dynamic interactions that differ from those that take place during capsid assembly (41).

The multifunctionality of viral proteins is becoming apparent (47). The oligomeric state and the existence of intrinsically disordered regions of VP3 might be the key to determining the molecular basis of its ability to generate a variety of functions.

Materials and Methods

Virion purification. IBDV virions were purified from QM7 quail muscle cells [American Type Culture Collection (ATCC) CRL-1962] infected with IBDV Soroa strain by ultracentrifugation on a 25% (w/w) sucrose cushion and a linear 25–50% sucrose gradient, as described (17). Alternatively, after pelleting through the sucrose cushion, particles were centrifuged through a CsCl equilibrium gradient. Six virus-containing bands were visible (E1-E6) and were collected separately by side puncturing (19).

Purification of RNP and dsRNA from IBDV virions. RNP complexes were purified from viral particles disrupted by dialysis against Tris-EDTA buffer (5 mM Tris-HCl pH 8.0, 5 mM EDTA) (72 h, 20ºC). The extract was concentrated in 0.5 ml 10 K Amicon ultracentrifuge tubes (Merck) and centrifuged twice on a glycerol step gradient, as reported (20). The middle fractions were dialyzed against Tris-EDTA buffer and analyzed by EM and immunoelectron microscopy using anti-VP3 antisera. dsRNA segments A and B were purified as described (19).

SDS-PAGE and Western blot. Concentrated gradient fractions (2-5 μl) were added to Laemmli sample buffer to a 1x final concentration (62.5 mM Tris–HCl, 2% SDS, 5% glycerol, 0.012% bromophenol blue, 2 mM dithiothreitol, pH 6.8), heated (3 min, 100°C), and resolved in 6-11% or 11% polyacrylamide gels, developed by Coomassie staining, washed with distilled water, and visualized with ethidium bromide. Alternatively, electrophoresis was followed by Western blot analyses using anti-VP2 or -VP3 antibodies.

Cryo-EM and image processing. Purified E1 particles (5 μl) were applied to Quantifoil R 2/2 holey grids, blotted, and plunged into liquid ethane. Samples were observed in a Tecnai G2 electron microscope. Images were recorded under low-dose conditions with a FEI Eagle CCD camera at a detector magnification of 69,444X (2.16 Å per pixel sampling rate). General

image processing operations were performed using Xmipp ([http://xmipp.cnb.csic.es/ (48)] and RELION (49) software packages integrated in the SCIPION platform (50), and with Bsoft [http://www.niams.nih.gov/rcn/labbranch/lsbr/software/bsoft/ (51)]. Graphics were produced by UCSF Chimera ([http://www.cgl.ucsf.edu/chimera/ (52)]. The Xmipp automatic picking routine was used to select 6,909 and 5,241 individual particle images of E1-1 and E1-2 capsids. E1-1 particles have a ring-like morphology with an empty central region, whereas E1-2 particles are homogeneously dark. A 0.7-5 μm defocus range was determined for each image with CTFfind4 (53) . Images were downsampled to a factor of 2, with a final sampling ratio of 4.32 Å/pixel. 2D classification with RELION, used to discard low-quality particles, was run for 25 iterations, with 60 classes, angular sampling of 5°, and a regularization parameter of T=1. 3D classification was run for 40 iterations, with four classes for each image set of E1-1 and E1-2 capsids, starting with an angular sampling of 3.7° decreased sequentially by 0.2° and a regularization parameter of T=2. The published IBDV structure (31), low-pass filtered to 35 Å, was used as initial reference for 3D classifications and refinements. Two classes were selected for E1-1 capsids, which contained 2,095 (E1-1A) and 2,027 (E1-1B) particles. The best two classes for E1-2 capsids were indistinguishable and were combined in a single map that contained 2,377 particles. Map resolutions were estimated from two independent half-datasets using the 0.3 criterion of the Fourier shell correlation (FSC), and the values for E1-1A, E1-1B and E1-2 maps were 28.2, 20.6 and 23.8 Å, respectively. Spherically averaged radial density profiles were calculated using Xmipp, normalized and scaled to match the fit between the cryo-EM maps. The UCSF Chimera fitting routine was used to dock the IBDV T=13 asymmetric unit [PDB entry 1WCE (16)] in the cryo-EM map, and icosahedral symmetry was applied. The mask generated was used to segment the E1-1A capsid.

Cryo-ET and image processing. Samples of E1-E6 particles were mixed with 10-nm colloidal gold particles (Aurion) and vitrified as above. Tomographic tilt series were recorded in a Tecnai-12 (FEI) electron microscope operating at 120 kV with a LaB_6 source and equipped with an energy filter (GIF 2002; Gatan). Images were recorded on a 2048 x 2048-pixel CCD camera (Gatan) at x53,600 magnification (5.6 Å/pixel) with ~4 μm underfocus, using the serialEM package (54). Tilt series were collected covering the range ±70° in 2° increments, with a total dose of ~75 electrons/$Å^2$ per series.

Data were preprocessed and aligned using IMOD software (55), with gold particles as fiducial markers. The final aligned tilt series were normalized and reconstructed using weighted back-projection algorithms implemented in Imod; 11, 10, 3, 4, 10 and 8 tomograms of E1, E2, E3, E4, E5 and E6 viral populations were reconstructed. Individual virus particles were manually selected, extracted and denoised by 100 iterations of anisotropic nonlinear diffusion (56) using Bsoft. A total of 247, 119, 95, 124, 475 and 457 particles were selected from E1, E2, E3, E4, E5 and E6 populations, respectively. The extracted viruses were aligned to a scale, low-pass filtered to a 35 Å 3D map of IBDV (31) using maximum likelihood procedures for tomography. A new density map was calculated and iteratively refined. Resolution of the averaged E1-E6 maps was in the 47–54 Å range. Spherically averaged radial density profiles of E1-E6 capsids were calculated with Xmipp, normalized, and scaled to match the fit between the cryo-ET maps.

Immunogold labeling of E1 and E5 T=13 capsids. (p)VP2 and VP3 were localized and identified by immunogold labeling on the outer or inner surfaces of E1 and E5 capsids, directly from sucrose- (E1 capsids) or CsCl-purified (E5 capsids) material or from material embedded in Lowicryl HM20. Fractions containing E1 and E5 capsids were pooled and centrifuged (240,000 x g, 2 h, 4°C), resuspended in 2% low melting point agarose in PES, and

391 subjected to mild fixation with a 4% paraformaldehyde solution containing 0.1%
392 glutaraldehyde in PBS (30 min, 4°C). Fixed capsids were washed in buffered glycerol and
393 quickly immersed in liquid ethane in the Leica EM CPC unit. The capsids were freeze-
394 substituted with 0.5% uranyl acetate in methanol (54 h, -90°C), then embedded in Lowicryl
395 HM20 resin (48 h at -40°C and 48 h at 20°C) in the Leica EM AFS2 unit. Thin sections (60–
396 70 nm) of particles were obtained with a Leica EM UC6 ultramicrotome and stained with
397 saturated uranyl acetate and lead citrate. Purified E1 and E5 capsids were applied to carbon-
398 coated grids, which were then blocked with 1% BSA-PBS (30 min). Polyclonal rabbit anti-
399 VP2 and -VP3 antisera, diluted 1/50 and 1/10 in 1% BSA-PBS, respectively, were incubated
400 (60 min), followed by three washes with PBS, and incubated with 1% BSA-PBS (15 min).
401 Goat anti-rabbit antiserum conjugated with 5-nm gold particles (1/50; BBInternational) was
402 added to the grid (45 min, room temperature). To remove nonspecific binding, the grids were
403 washed three times with PBS followed by four washes with water. The grids were then
404 negatively stained with 2% (w/v) aqueous uranyl acetate. Immunogold was detected on
405 ultrathin sections of E1 and E5 capsids at room temperature using rabbit polyclonal anti-VP2
406 and -VP3 antisera, essentially as described above.
407 **Atomic force microscopy.** AFM experiments were as described (41). Surface-attached
408 capsids were imaged in physiological conditions using jumping mode. We used 0.05 N/m
409 force constant Olympus silicon nitride cantilevers. Data were analyzed with WSxM software
410 (57). Capsid position was determined in low resolution images (128 x 128 pixels) at maximal
411 scanning force (<100 pN). The applied force was calibrated by single force vs. Z piezo
412 displacement curves (FZ) on a highly oriented pyrolytic graphite surface (HOPG) next to the
413 capsid. After individual details of capsids were resolved, indentation measurements were

414 performed to quantitate particle elastic response. A series of three to five successive FZ
415 curves was obtained, and measurements performed on ~30 particles per population.
416 **FE simulations of IBDV capsids.** FE simulations of AFM indentation were done using
417 COMSOL Multiphysics 4.3 (Comsol, Stockholm, Sweden). In all cases, the capsid wall was
418 considered as a spherical shell made of a homogenous material, with Young's modulus
419 E = 120 MPa and Poisson ratio ν = 0.3 (a standard value for protein-like materials). This
420 model capsid was placed on a hard, flat substrate and indented by a hard spherical object with
421 radius R_{in}=15 nm to mimic the AFM tip. The system was simulated using a 2D axisymmetric
422 model meshed with over 3000-6000 triangular elements. Contacts were implemented between
423 the shell and the tip as well as the supporting surface during indentation, with a contact-
424 penalty stiffness method based on the manufacturer's manual. A parametric, non-linear solver
425 was used to simulate the stepwise lowering of the tip onto the capsid. The spring constant was
426 derived from a linear fit of force vs indentation for small indentations. For the T=1 capsid, the
427 spring constant was measured as the slope of the force indentation curve at 2 nm, and for the
428 empty T=13 E1 capsid, at 4 nm. These values were chosen to mimic the typical indentations
429 used in the experiments.
430 **Data deposition.** The E1-1A, E1-1B and E1-2 cryo-EM maps are deposited in the Electron
431 Microscopy Data Bank (EMDB, http://www.ebi.ac.uk/pdbe/emdb) with accession nº emd-
432 3507, emd-3509 and emd-3510, respectively. E1-E6 cryo-ET averaged maps are deposited in
433 the EMDB with accession nº emd-3511-emd-3516.
434

Acknowledgments

We thank Pedro J de Pablo for technical support and stimulating discussions for AFM experiments and Santiago Casado for technical assistance with AFM. We also thank the CNB-CSIC Electron Microscopy Service for technical assistance with immunoelectron microscopy, and Catherine Mark for editorial assistance. CPM was a PhD fellow of the La Caixa Foundation International Fellowship Program (La Caixa/CNB). This work was supported by grants from the Spanish Ministry of Economy and Competitivity (BFU2013-43149-R to DL, FIS2015-67837-P to DR, MAT2015-66605-P to JM, BFU2014-54181 to JLC and BFU2017-88736-R to JRC), the Generalitat de Catalunya (AGAUR 2014-SGR-922 to DR), the Comunidad Autónoma de Madrid (S2013/MIT-2850 to JLC and S2013/MIT-2807 to JRC), and the NIH Intramural Research Program of the Center for Information Technology (to BLT), and of the National Institute of Arthritis, Musculoskeletal and Skin Diseases (to ACS).

References

1. **Abrescia NG, Bamford DH, Grimes JM, Stuart DI.** 2012. Structure unifies the viral universe. Annu Rev Biochem **81:**795-822.
2. **Bamford DH, Grimes JM, Stuart DI.** 2005. What does structure tell us about virus evolution? Curr Opin Struct Biol **15:**655-663.
3. **Rossmann M, Johnson J.** 1989. Icosahedral RNA Virus Structure. Annu Rev Biochem **58:**533-573.
4. **Bahar MW, Graham SC, Chen RA, Cooray S, Smith GL, Stuart DI, Grimes JM.** 2011. How vaccinia virus has evolved to subvert the host immune response. J Struct Biol **175:**127-134.
5. **Hyun JK, Coulibaly F, Turner AP, Baker EN, Mercer AA, Mitra AK.** 2007. The structure of a putative scaffolding protein of immature poxvirus particles as determined by electron microscopy suggests similarity with capsid proteins of large icosahedral DNA viruses. J Virol **81:**11075-11083.
6. **Steven AC, Heymann JB, Cheng N, Trus BL, Conway JF.** 2005. Virus maturation: dynamics and mechanism of a stabilizing structural transition that leads to infectivity. Curr Opin Struct Biol **15:**227-236.
7. **Feiss M, Rao VB.** 2012. The bacteriophage DNA packaging machine. Adv Exp Med Biol **726:**489-509.
8. **Krupovic M, Bamford DH.** 2011. Double-stranded DNA viruses: 20 families and only five different architectural principles for virion assembly. Curr Opin Virol **1:**118-124.
9. **Veesler D, Johnson JE.** 2012. Virus maturation. Annu Rev Biophys **41:**473-496.
10. **Hong C, Oksanen HM, Liu X, Jakana J, Bamford DH, Chiu W.** 2014. A structural model of the genome packaging process in a membrane-containing double stranded DNA virus. PLoS Biol **12:**e1002024.
11. **Patton JT.** 2008. Segmented double-stranded RNA viruses: structure and molecular biology. Caister Academic Press, Norfolk. UK.
12. **Zhang X, Ding K, Yu X, Chang W, Sun J, Zhou ZH.** 2015. In situ structures of the segmented genome and RNA polymerase complex inside a dsRNA virus. Nature **527:**531-534.
13. **Liu H, Cheng L.** 2015. Cryo-EM shows the polymerase structures and a nonspooled genome within a dsRNA virus. Science **349:**1347-1350.
14. **Sung PY, Roy P.** 2014. Sequential packaging of RNA genomic segments during the assembly of Bluetongue virus. Nucleic Acids Res **42:**13824-13838.
15. **Fajardo T, Jr., Sung PY, Roy P.** 2015. Disruption of Specific RNA-RNA Interactions in a Double-Stranded RNA Virus Inhibits Genome Packaging and Virus Infectivity. PLoS Pathog **11:**e1005321.
16. **Coulibaly F, Chevalier C, Gutsche I, Pous J, Navaza J, Bressanelli S, Delmas B, Rey FA.** 2005. The birnavirus crystal structure reveals structural relationships among icosahedral viruses. Cell **120:**761-772.
17. **Saugar I, Luque D, Ona A, Rodriguez JF, Carrascosa JL, Trus BL, Caston JR.** 2005. Structural polymorphism of the major capsid protein of a double-stranded RNA virus: an amphipathic alpha helix as a molecular switch. Structure **13:**1007-1017.
18. **Caston JR, Martinez-Torrecuadrada JL, Maraver A, Lombardo E, Rodriguez JF, Casal JI, Carrascosa JL.** 2001. C terminus of infectious bursal disease virus major

capsid protein VP2 is involved in definition of the T number for capsid assembly. J Virol **75:**10815-10828.
19. **Luque D, Rivas G, Alfonso C, Carrascosa JL, Rodriguez JF, Caston JR.** 2009. Infectious bursal disease virus is an icosahedral polyploid dsRNA virus. Proc Natl Acad Sci USA **106:**2148-2152.
20. **Luque D, Saugar I, Rejas MT, Carrascosa JL, Rodriguez JF, Caston JR.** 2009. Infectious Bursal disease virus: ribonucleoprotein complexes of a double-stranded RNA virus. J Mol Biol **386:**891-901.
21. **Birghan C, Mundt E, Gorbalenya AE.** 2000. A non-canonical lon proteinase lacking the ATPase domain employs the Ser-Lys catalytic dyad to exercise broad control over the life cycle of a double-stranded RNA virus. EMBO J **19:**114-123.
22. **Feldman AR, Lee J, Delmas B, Paetzel M.** 2006. Crystal structure of a novel viral protease with a serine/lysine catalytic dyad mechanism. J Mol Biol **358:**1378-1389.
23. **Kochan G, Gonzalez D, Rodriguez JF.** 2003. Characterization of the RNA-binding activity of VP3, a major structural protein of Infectious bursal disease virus. Arch Virol **148:**723-744.
24. **van Cleef KW, van Mierlo JT, Miesen P, Overheul GJ, Fros JJ, Schuster S, Marklewitz M, Pijlman GP, Junglen S, van Rij RP.** 2014. Mosquito and Drosophila entomobirnaviruses suppress dsRNA- and siRNA-induced RNAi. Nucleic Acids Res **42:**8732-8744.
25. **Casanas A, Navarro A, Ferrer-Orta C, Gonzalez D, Rodriguez JF, Verdaguer N.** 2008. Structural insights into the multifunctional protein VP3 of birnaviruses. Structure **16:**29-37.
26. **Garriga D, Navarro A, Querol-Audi J, Abaitua F, Rodriguez JF, Verdaguer N.** 2007. Activation mechanism of a noncanonical RNA-dependent RNA polymerase. Proc Natl Acad Sci USA **104:**20540-20545.
27. **Ferrero D, Garriga D, Navarro A, Rodriguez JF, Verdaguer N.** 2015. Infectious Bursal Disease Virus VP3 Upregulates VP1-Mediated RNA-Dependent RNA Replication. J Virol **89:**11165-11168.
28. **Saugar I, Irigoyen N, Luque D, Carrascosa JL, Rodriguez JF, Caston JR.** 2010. Electrostatic interactions between capsid and scaffolding proteins mediate the structural polymorphism of a double-stranded RNA virus. J Biol Chem **285:**3643-3650.
29. **Galloux M, Libersou S, Alves ID, Marquant R, Salgado GF, Rezaei H, Lepault J, Delmas B, Bouaziz S, Morellet N.** 2010. NMR structure of a viral peptide inserted in artificial membranes: a view on the early steps of the birnavirus entry process. J Biol Chem **285:**19409-19421.
30. **Ortin J, Martin-Benito J.** 2015. The RNA synthesis machinery of negative-stranded RNA viruses. Virology **479-480:**532-544.
31. **Luque D, Saugar I, Rodriguez JF, Verdaguer N, Garriga D, Martin CS, Velazquez-Muriel JA, Trus BL, Carrascosa JL, Caston JR.** 2007. Infectious bursal disease virus capsid assembly and maturation by structural rearrangements of a transient molecular switch. J Virol **81:**6869-6878.
32. **Ahlquist P.** 2005. Virus evolution: fitting lifestyles to a T. Curr Biol **15:**R465-R467.
33. **Gibbons MM, Klug WS.** 2007. Nonlinear finite-element analysis of nanoindentation of viral capsids. Phys Rev E Stat Nonlin Soft Matter Phys **75:**031901.
34. **de Pablo PJ, Mateu MG.** 2013. Mechanical properties of viruses. Subcell Biochem **68:**519-551.

35. **Alfson KJ, Avena LE, Beadles MW, Staples H, Nunneley JW, Ticer A, Dick EJ, Jr., Owston MA, Reed C, Patterson JL, Carrion R, Jr., Griffiths A.** 2015. Particle-to-PFU ratio of Ebola virus influences disease course and survival in cynomolgus macaques. J Virol **89:**6773-6781.
36. **Cardone G, Newcomb WW, Cheng N, Wingfield PT, Trus BL, Brown JC, Steven AC.** 2012. The UL36 tegument protein of herpes simplex virus 1 has a composite binding site at the capsid vertices. J Virol **86:**4058-4064.
37. **Steven AC, Baumeister W, Johnson LN, OPerham RN.** 2016. Molecular biology of assemblies and machines. Garland Science, New york, London.
38. **Garriga D, Querol-Audi J, Abaitua F, Saugar I, Pous J, Verdaguer N, Caston JR, Rodriguez JF.** 2006. The 2.6-Angstrom structure of infectious bursal disease virus-derived T=1 particles reveals new stabilizing elements of the virus capsid. J Virol **80:**6895-6905.
39. **Irigoyen N, Caston JR, Rodriguez JF.** 2012. Host proteolytic activity is necessary for infectious bursal disease virus capsid protein assembly. J Biol Chem **287:**24473-24482.
40. **Irigoyen N, Garriga D, Navarro A, Verdaguer N, Rodriguez JF, Caston JR.** 2009. Autoproteolytic activity derived from the infectious bursal disease virus capsid protein. J Biol Chem **284:**8064- 8072.
41. **Mertens J, Casado S, Mata CP, Hernando-Perez M, de Pablo PJ, Carrascosa JL, Caston JR.** 2015. A protein with simultaneous capsid scaffolding and dsRNA-binding activities enhances the birnavirus capsid mechanical stability. Sci Rep **5:**13486.
42. **Schneemann A.** 2006. The structural and functional role of RNA in icosahedral virus assembly. Annu Rev Microbiol **60:**51-67.
43. **Lombardo E, Maraver A, Cast n JR, Rivera J, Fernandez-Arias A, Serrano A, Carrascosa JL, Rodriguez JF.** 1999. VP1, the putative RNA-dependent RNA polymerase of infectious bursal disease virus, forms complexes with the capsid protein VP3, leading to efficient encapsidation into virus-like particles. J Virol **73:**6973-6983.
44. **Chen DH, Baker ML, Hryc CF, DiMaio F, Jakana J, Wu W, Dougherty M, Haase-Pettingell C, Schmid MF, Jiang W, Baker D, King JA, Chiu W.** 2011. Structural basis for scaffolding-mediated assembly and maturation of a dsDNA virus. Proc Natl Acad Sci USA **108:**1355-1360.
45. **Prevelige PE, Fane BA.** 2012. Building the machines: scaffolding protein functions during bacteriophage morphogenesis. Adv Exp Med Biol **726:**325-350.
46. **Suhanovsky MM, Teschke CM.** 2015. Nature's favorite building block: Deciphering folding and capsid assembly of proteins with the HK97-fold. Virology **479-480:**487-497.
47. **Jayaraman B, Smith AM, Fernandes JD, Frankel AD.** 2016. Oligomeric viral proteins: small in size, large in presence. Crit Rev Biochem Mol Biol **51:**379-394.
48. **de la Rosa-Trevin JM, Oton J, Marabini R, Zaldivar A, Vargas J, Carazo JM, Sorzano CO.** 2013. Xmipp 3.0: an improved software suite for image processing in electron microscopy. J Struct Biol **184:**321-328.
49. **Scheres SH.** 2012. A Bayesian view on cryo-EM structure determination. J Mol Biol **415:**406-418.
50. **de la Rosa-Trevin JM, Quintana A, Del Cano L, Zaldivar A, Foche I, Gutierrez J, Gomez-Blanco J, Burguet-Castell J, Cuenca-Alba J, Abrishami V, Vargas J, Oton J, Sharov G, Vilas JL, Navas J, Conesa P, Kazemi M, Marabini R, Sorzano CO, Carazo JM.** 2016. Scipion: A software framework toward integration, reproducibility and validation in 3D electron microscopy. J Struct Biol **195:**93-99.

51. **Heymann JB, Belnap DM.** 2007. Bsoft: image processing and molecular modeling for electron microscopy. J Struct Biol **157:**3-18.
52. **Pettersen EF, Goddard TD, Huang CC, Couch GS, Greenblatt DM, Meng EC, Ferrin TE.** 2004. UCSF Chimera--a visualization system for exploratory research and analysis. J Comput Chem **25:**1605-1612.
53. **Rohou A, Grigorieff N.** 2015. CTFFIND4: Fast and accurate defocus estimation from electron micrographs. J Struct Biol **192:**216-221.
54. **Mastronarde DN.** 2005. Automated electron microscope tomography using robust prediction of specimen movements. J Struct Biol **152:**36-51.
55. **Kremer JR, Mastronarde DN, McIntosh JR.** 1996. Computer visualization of three-dimensional image data using IMOD. J Struct Biol **116:**71-76.
56. **Frangakis AS, Hegerl R.** 2001. Noise reduction in electron tomographic reconstructions using nonlinear anisotropic diffusion. J Struct Biol **135:**239-250.
57. **Horcas I, Fernandez R, Gomez-Rodriguez JM, Colchero J, Gomez-Herrero J, Baro AM.** 2007. WSXM: a software for scanning probe microscopy and a tool for nanotechnology. Rev Sci Instrum **78:**013705.

605 **Figure legends**

606 **FIG 1**. Purification and biochemical analysis of IBDV natural populations. (A) A CsCl linear
607 gradient for IBDV purification, illuminated from the bottom after centrifugation to
608 equilibrium, containing at least six IBDV fractions (E1-E6, from top to bottom). E1-E6 bands
609 contain 3, 5, 12, 16, 48 and 16% of the total virion particles. E6 have a slightly higher
610 buoyant density, probably due to the presence of unspecific viral RNA fragments or, even,
611 cellular RNA as described in other viruses; E4-E5 populations that contain more than 1
612 complete genome account for ~80% of total particles. (B) Coomassie blue- (left) and
613 ethidium bromide-stained (right) SDS-PAGE gel of E1-E6 populations (on the same 11%
614 gel). Molecular size markers (x 10^{-3} Da) are shown at left; bands corresponding to proteins
615 VP1, pVP2, VP2, VP3 and VP4 and dsRNA are indicated.

616 **FIG 2**. Cryo-electron tomography of T=13 capsids from E1-E6 IBDV populations. (A, B)
617 Sections through a cryotomogram of a field of E1 (A) and E5 (B) IBDV populations. (A) At
618 least two classes of E1 particles can be distinguished, E1 particles with an irregular thickened
619 shell and empty central region, and E1 particles with uniform density in the capsid interior.
620 T=1 and T=7 capsids are indicated. (B) E5 particles are uniformly full capsids. A contaminant
621 T=1 capsid is indicated. Bar = 50 nm. (C) Gallery of sections from E1 capsid tomograms.
622 Sections i-iii are empty E1 particles with a thickened capsid shell (50% of total); section iv is
623 an empty E1 particle with collapsed internal material, and section v shows an E1 particle with
624 homogeneous internal density (~36%). (D) Gallery of sections of E2, E3, E4, E5 and E6
625 IBDV capsids (left to right). Hexagon diagrams show the amount of RNP (dots) packed
626 within the particle (inset, bottom left). Bar = 50 nm. (E) Surface-shaded representations of the
627 outer surface, viewed along an icosahedral 2-fold axis contoured at 1 σ above the mean
628 density, of the averaged E1-E6 T=13 capsids (top row). Transverse central sections of the

3DR (bottom row, left) and 73 Å-thick slabs (bottom row, right) contoured at 0.5 σ above the mean density to highlight internal content. Dark shading indicates higher density. Arrows indicate contacts between the E1 T=13 capsid shell and the underlying shell. Bar, 100 Å. (F) Radial density profiles from averaged 3D maps of E1-E6 particles. E2-E6 profiles are practically superimposable along all radii. E1 and E2-E6 profiles are only superimposable at the protein shell (radius ~260 to 350 Å). Note that the E1 profile has a less intense Fresnel ring (at a radius of ~250 Å, arrow) due to numerous contacts between the capsid and the underlying layers (centered at a radius of ~225 Å), and the E1 internal volume is empty.

FIG 3. Biochemical characterization and 3D cryo-EM reconstructions of IBDV E1 capsids. (A-C) The E1 pooled preparation was ultracentrifuged through a sucrose gradient, 12 fractions were collected, concentrated, analyzed by SDS-PAGE, and developed by Coomassie staining (A) or by Western blot using anti-VP2 (B) and -VP3 (C) antibodies. Direction of sedimentation was right to left, with fraction 12 at the gradient top. Molecular size markers (x 10^{-3} Da) at left; pVP2, VP2 and VP3 bands are indicated. (D) Electron microscopy of negatively stained E1 particles. Left, purified E1 particles after ultracentrifugation in a CsCl gradient. Center, T=13 capsid-enriched E1 fraction obtained after consecutive ultracentrifugation in a sucrose gradient, corresponding to central fractions (fractions 6-7). Right, T=1 capsid-enriched E1 fraction obtained after consecutive ultracentrifugation in a sucrose gradient, corresponding to upper fractions (fractions 10-11). (E) Cryo-electron micrograph of twice-purified E1 T=13 capsids from fractions 6-7 in (A) and (D). Red arrows indicate E1-1 particles whose morphology is characterized by a thickened capsid wall with an empty central region; blue arrows indicate E1-2 particles that are homogeneously dark. Bar, 100 nm. (F) Radial density profiles from averaged 3D maps of E1-1A (red), E1-1B (green) and E1-2 (blue) particles. A radial profile calculated from a previous IBDV map is included

as control (black). Note that the VP3 layer (centered at a ~225 Å radius), as well as the Fresnel ring at the inner capsid surface (at a ~250 Å radius), decrease from E1-1A to E1-1B to E1-2. E1-1A and E1-1B capsids are completely empty in the central region (to a ~150 Å radius). (G) Radially color-coded inner (top row) and outer (bottom row) surfaces of E1-1A (left), E1-1B (center) and E1-2 capsids (right), viewed along an icosahedral twofold axis (T=13 shell in yellow; VP3 density, orange). Maps are calculated with (left halves) and without (right halves) icosahedral symmetry, and are contoured at 1.25 σ above the mean density. Bar, 100 Å.

FIG 4. Structural comparison of T=13 capsids from an E1 natural population. (A-D) Transverse central sections from the 3D reconstructions of E1-1A (A), E1-1B (B), E1-2 (C) and IBDV (D) particles, viewed along an icosahedral twofold axis and filtered at 30 Å resolution (with icosahedral symmetry, left half), or at 40 Å resolution (without imposing icosahedral symmetry, right half). (E-H) Two-dimensional reprojected views of the 3D reconstructions viewed along a twofold icosahedral axis of E1-1A (E), E1-1B (F), E1-2 (G) and IBDV (H) particles, after computationally removing their internal content (with and without icosahedral symmetry; left and right halves, respectively). Reprojections are basically identical. (I-L) Two-dimensional reprojected views of the 3D reconstructions viewed along a twofold icosahedral axis of E1-1A (I), E1-1B (J), E1-2 (K) and IBDV (L) particles, without removing internal content (with and without icosahedral symmetry; left and right halves, respectively).

FIG 5. Immunogold labeling of pVP2/VP2 and VP3 on the outer and inner surfaces of E1 and E5 T=13 capsids. (A) E5 T=13 capsids were attached to coated grids and incubated with polyclonal rabbit anti-VP2 (left half) or -VP3 antisera (right half). Bound antibody was detected with goat anti-rabbit immunoglobulin conjugated to 5-nm colloidal gold particles. (B-C) Immunogold localization of pVP2/VP2 (B) and VP3 (C) of resin-embedded E5 T=13

677 capsids. (D) E1 T=13 capsids were attached to coated grids and incubated with polyclonal
678 rabbit anti-VP2 (left half) or -VP3 antisera (right half). Bound antibody was detected as in A.
679 (E-F) Immunogold localization of pVP2/VP2 (E) and VP3 (F) of resin-embedded E1 T=13
680 capsids. Location of pVP2/VP2 (B and E) and VP3 (C and F) with polyclonal anti-VP2
681 and -VP3 antisera and a 5-nm colloidal gold conjugate on LR-WHITE sections. Cytochemical
682 controls with the preimmune sera for VP2 and VP3 showed no label. Bars, 100 nm.
683 **FIG 6**. Mechanical rigidity of E1 T=13 and T=1 capsids and finite element simulations that
684 mimic AFM indentations. (A, B) Histograms of slopes of the indentation curves for E1 T=13
685 (A) and T=1 capsids (B), showing rigidity values (spring constant, k) for individual particles
686 after nanoindentation. The k value for each population was calculated by Gaussian fits $K_{E1-T=13}$ = 0.347 ± 0.104 N/m (A) and $K_{T=1}$= 0.327 ± 0.085 N/m (B). For E1 T=1 capsids, $K_{E1-T=1}$
688 = 0.309 ± 0.127 N/m. AFM images of individual T=13 (bar, 200 Å) and T=1 particles (bar,
689 100 Å) are shown (inset, top right). (C) Force-indentation curves obtained by FE simulation
690 to mimic AFM experiments for IBDV T=13 and T=1 capsids. Values shown for the T=1
691 capsid (black), T=13 capsid using R=35 nm and an 8 nm-thick layer (red), and T=13 capsid
692 with thickness increased to 11.5 nm (green) to match the spring constant measured in the
693 experiments.
694

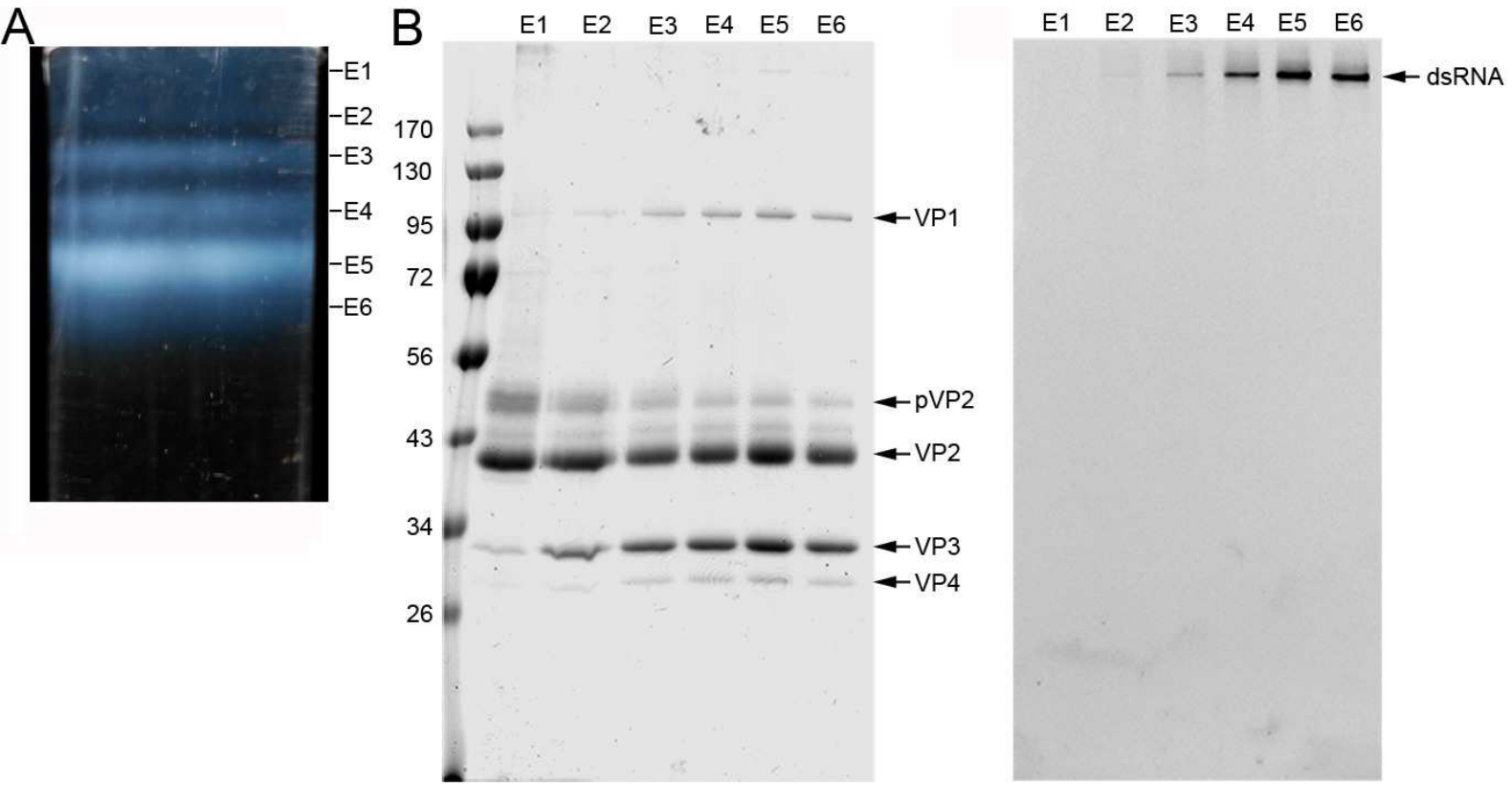
A
E1
E2
E3
E4
E5
E6
B
E1
E2
E3
E4
E5
E6
170
130
95
72
56
43
34
26
VP1
pVP2
VP2
VP3
VP4
E1
E2
E3
E4
E5
E6
dsRNA

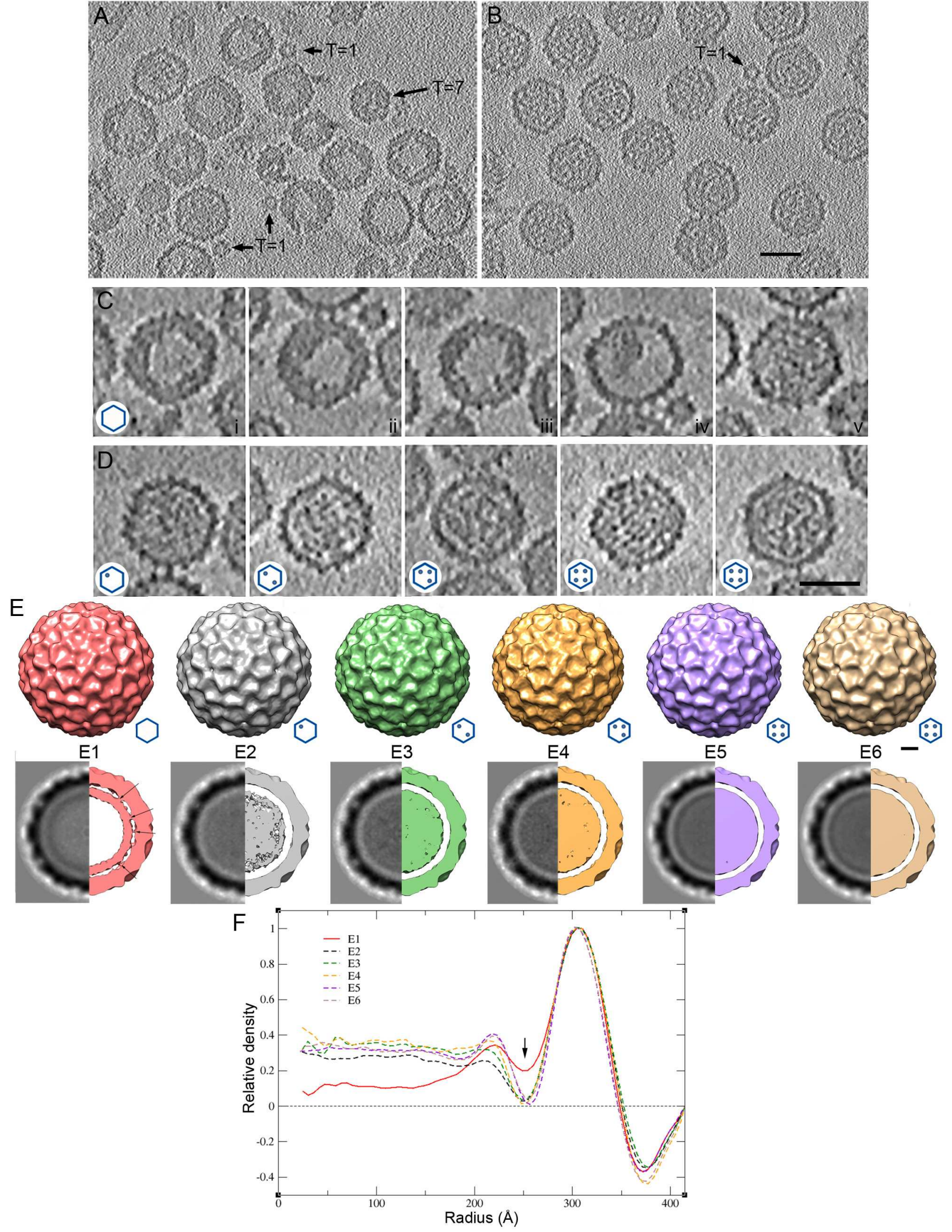
A
T=1
T=7
T=1
B
T=1
C
i
ii
iii
iv
v
D
E
E1
E2
E3
E4
E5
E6
F
E1
E2
E3
E4
E5
E6
Relative density
1
0.8
0.6
0.4
0.2
0
-0.2
-0.4
0
100
200
300
400
Radius (Å)

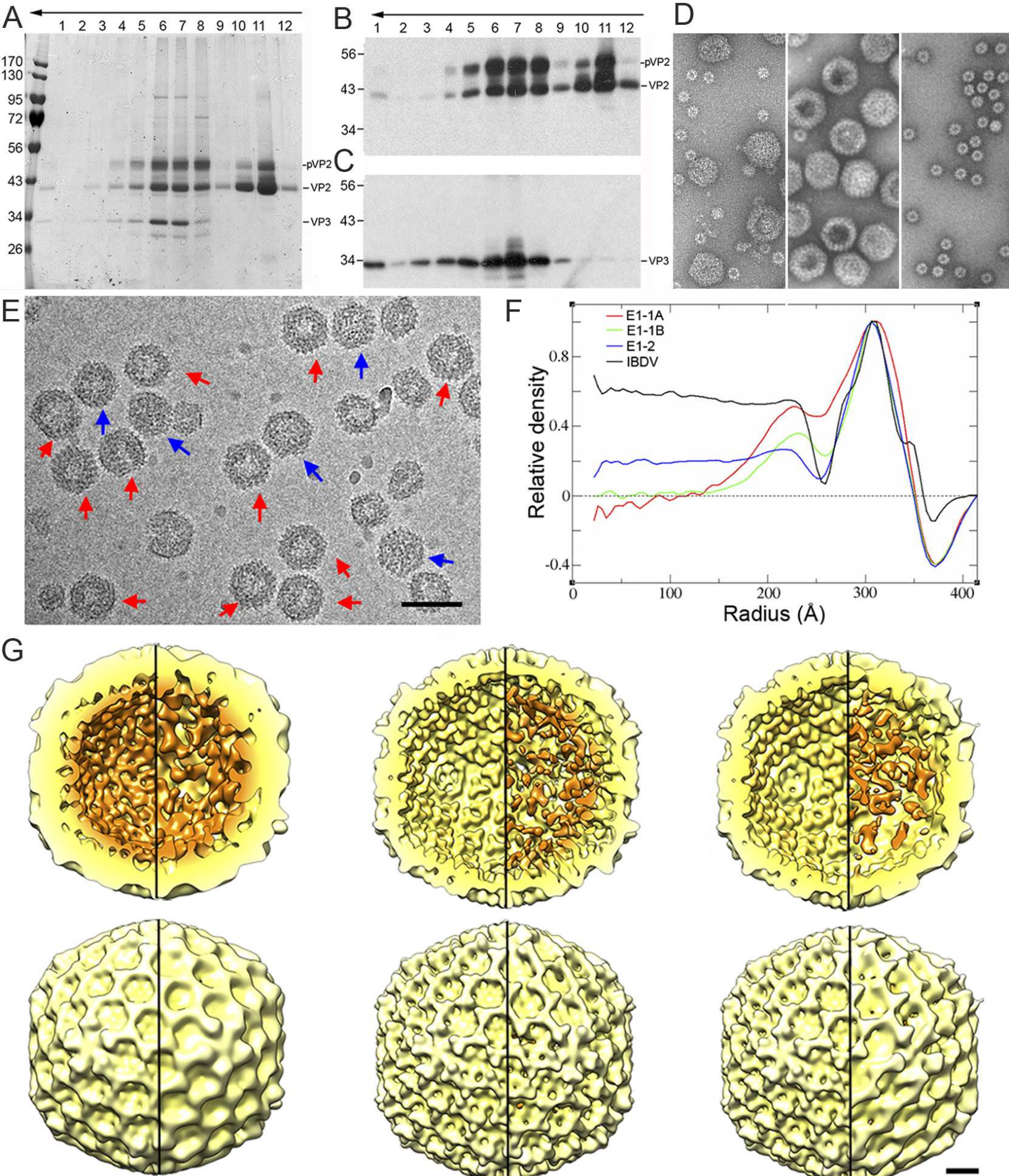
A
1 2 3 4 5 6 7 8 9 10 11 12
170
130
95
72
56
43
34
26
pVP2
VP2
VP3
B
1 2 3 4 5 6 7 8 9 10 11 12
56
43
34
pVP2
VP2
C
56
43
34
VP3
D
E
F
E1-1A
E1-1B
E1-2
IBDV
Relative density
0.8
0.4
0
-0.4
0
100
200
300
400
Radius (Å)
G

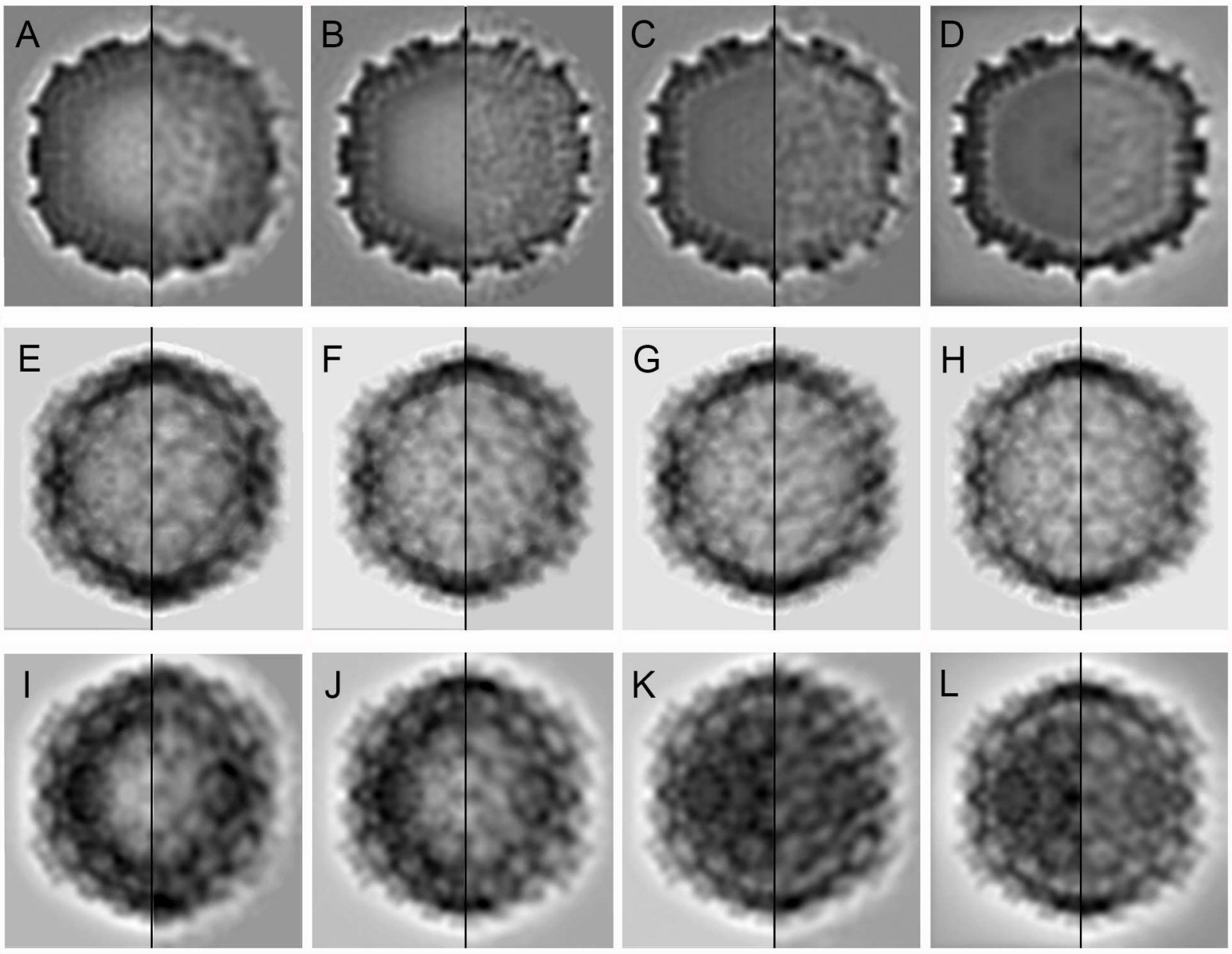
A
B
C
D
E
F
G
H
I
J
K
L

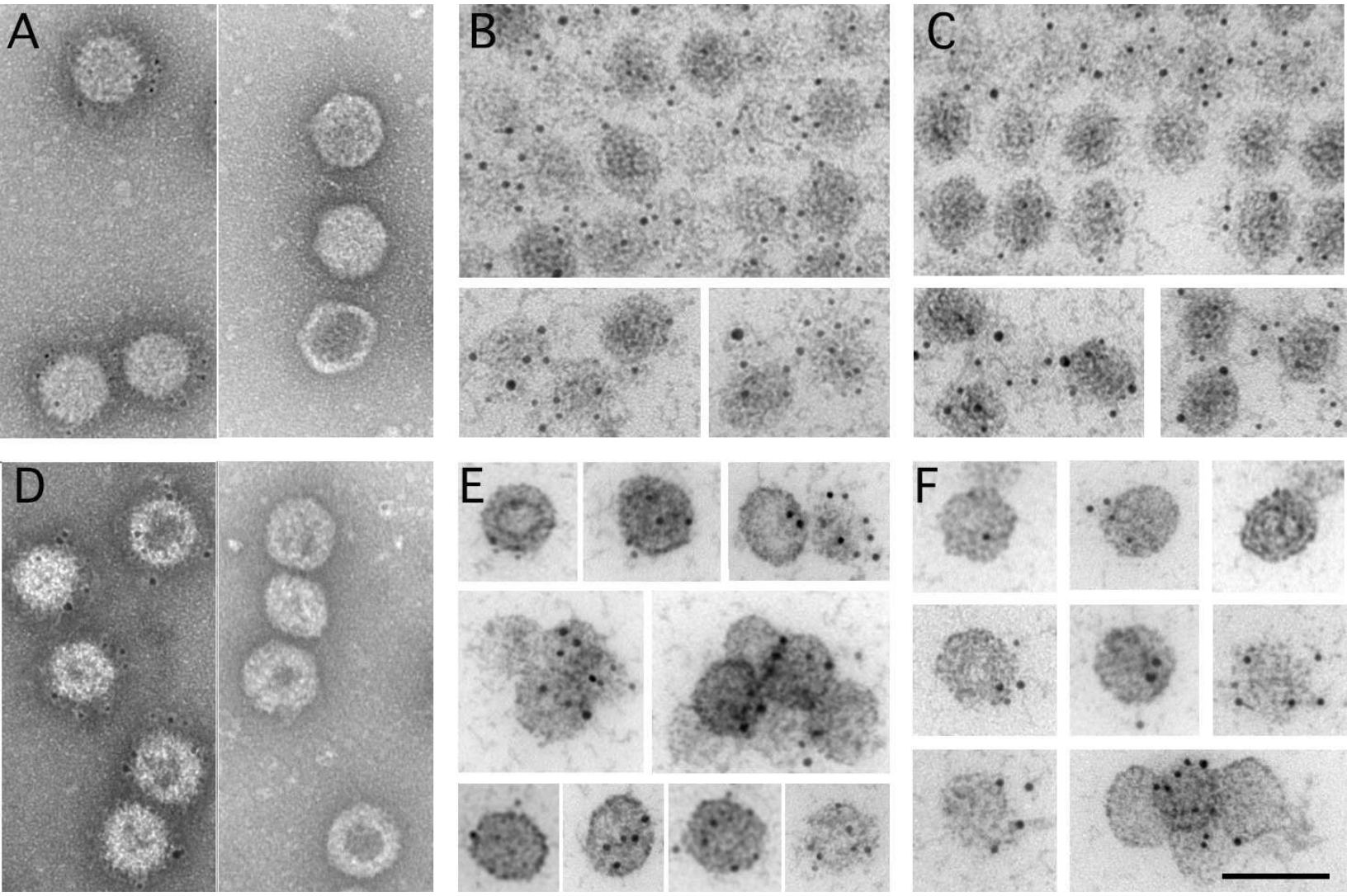
A
B
C
D
E
F

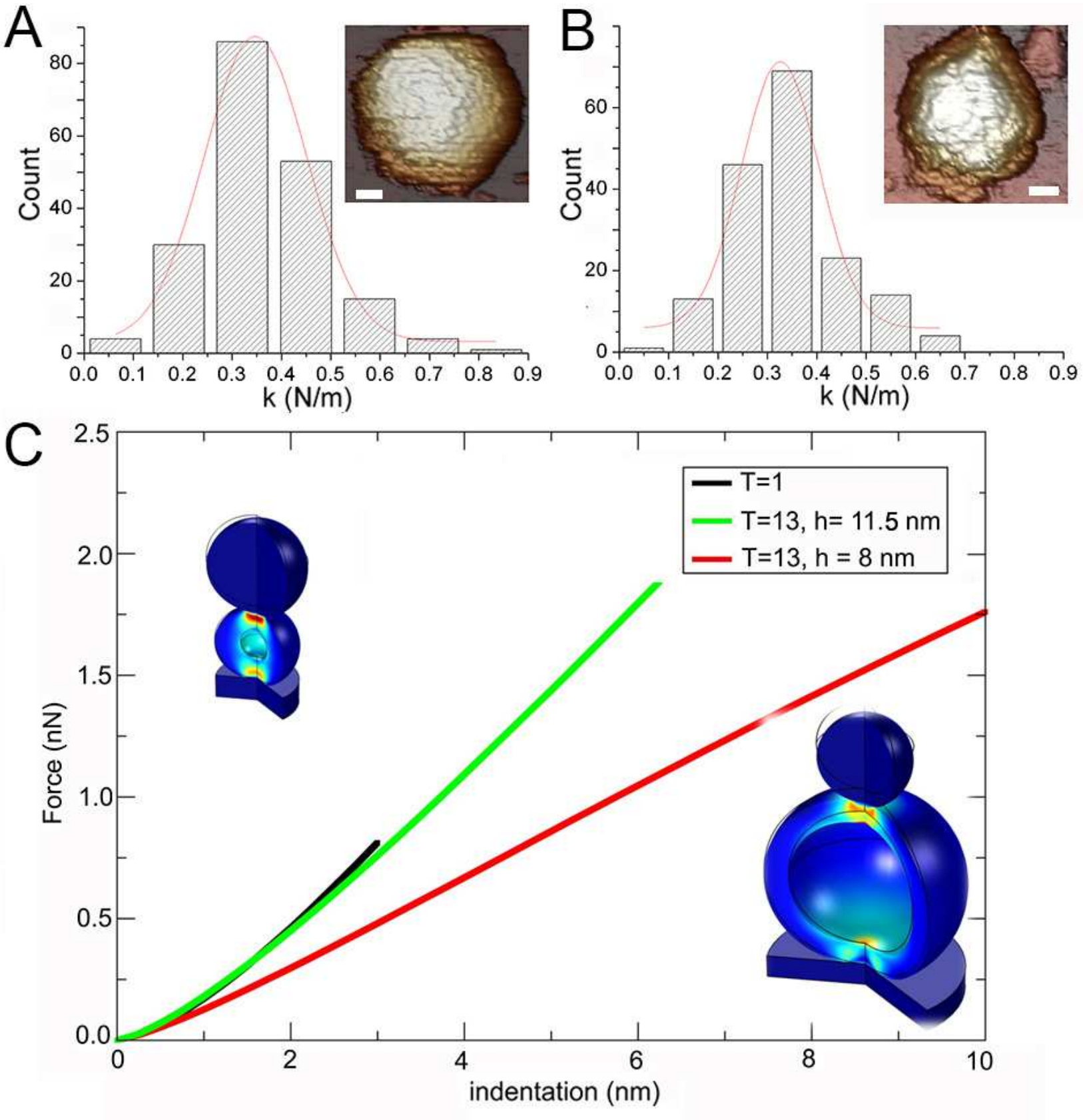
A
Count
k (N/m)
B
Count
k (N/m)
C
T=1
T=13, h= 11.5 nm
T=13, h = 8 nm
Force (nN)
indentation (nm)